Publisher: GSA
Journal: GEOL: Geology
DOI:10.1130/G39892.1

Diatom ooze: Crucial for the generation of submarine mega-slides?

Morelia Urlaub[1], Jacob Geersen[1], Sebastian Krastel[2], and Tilmann Schwenk[3]

[1]Geomar Helmholtz Centre for Ocean Research Kiel, 24148 Kiel, Germany

[2]Institute of Geosciences, Kiel University, 24118 Kiel, Germany

[3]MARUM–Center for Marine Environmental Sciences and Faculty of Geosciences, University of Bremen, 28359 Bremen, Germany

ABSTRACT

Numerous studies invoke weak layers to explain the occurrence of submarine mega-slides (>100 km^3), in particular those on very gentle slopes (<3°). Failure conditions are thought to be met only within this layer, which is embedded between stable sediments. Although key to understanding failure mechanisms, little is known about the nature and composition of such weak layers, mainly because they are destroyed with the landslides. This study is the first to place detailed constraints on the weak layer for one of the submarine mega-slides that occurred on the nearly flat subtropical Northwest African continental slopes. Integrating results from the Ocean Drilling Program with high resolution seismic reflection data we show that the failure surfaces traced into the undisturbed sedimentary sequence coincide with thin (<10 m) diatom ooze layers capped by clay. As diatom oozes are common on many continental margins, we suggest a new margin-independent failure mechanism to explain submarine mega-slides at low gradient continental slopes globally. Diatom oozes are susceptible to building up excess pore fluid during burial due to their high compressibility and water content. If a

low permeable clay cap prevents upward drainage, excess pore pressures accumulate in the ooze-clay interface causing the shearing resistance to increase at a lower rate than the shear stress until failure can occur. Changes in global climate affect the abundance of diatoms and thus formation of diatom oozes, thereby preconditioning the sediments for failure. However, the actual timing of failure is independent of environmental changes.

INTRODUCTION

Submarine landslides are the largest mass movements on Earth, and they can be far larger than any terrestrial slope failure (Masson et al., 2006). For example, the giant Storegga Slide offshore Norway that occurred ~8,150 years ago moved >3000 km^3 of slope sediments. It triggered a North Atlantic wide tsunami that inundated surrounding coasts to heights of up to 20 m (Bondevik et al., 2005). For comparison, collapse of Mt St Helens volcano in 1980 involved ~3 km^3 of rock material (Voight et al., 1983), while the annual global flux of sediment from rivers into the ocean is ~11 km^3 (Milliman and Syvitski, 1992).

Submarine landslides occur globally, but the largest (>100 km^3) events have occurred along gently inclined (<3°) slopes on passive continental margins in areas with thick fine-grained sedimentary deposits (Masson et al., 2006). The majority of these mega-slides are translational, such that failure takes place along bedding-parallel surfaces (called glide planes). Commonly, sliding involves several glide planes at different stratigraphic depths, leaving behind staircase morphologies. It appears that the wide spatial extent of these landslides is due to the absence of major morphological breaks and geological discontinuities over wide areas. This suggests that distinct ‘weak layers’ capable of accommodating slope failure may form over thousands of square kilometers (Masson et al., 2010).

The most compelling constraints on weak layers come from Finneidfjord in Norway (a thin turbidite of stratified sand and clay; L'Heureux et al., 2012) and the catastrophic 1979 Nice airport landslide (a sensitive clay layer that was weakened by pore fluid flow; Dan et al., 2007). However, these are small submarine landslides that occurred on relatively steep slopes. For giant submarine landslides on very gentle slopes the composition and nature of weak layers is poorly documented. This is because sediment cores that penetrate the failure surface typically show landslide debris directly overlying undisturbed older sediment. The weak layer has thus been destroyed by slide movement, and the sediment from which the weak layer consisted has vanished with the landslide. To date, the only detailed study on a weak layer of a giant submarine landslide comes from the well-studied Storegga Slide, where the weak layer corresponds to glacial marine clay with strain softening behavior (Kvalstad et al., 2005).

Here, we provide the first detailed study of a weak layer associated with a submarine mega-slide at a subtropical continental margin: the Cap Blanc Slide off Northwest Africa (Fig. 1). Using high resolution seismic reflection data, we trace the failure surfaces of three landslides to Ocean Drilling Program (ODP) Site 658 (20°44′57'' N, 18°34′51''W, 2263 m water depth). The ODP core recovered ~300 m of sediment including one glide plane as well as undisturbed sedimentary sequences including two failure surfaces linked to two landslides that have occurred at some distance to the core. This setting thus provides the unique opportunity to identify the weak layers responsible for the Cap Blanc Slide. We then develop a novel and widely applicable model for the landslide failure mechanism, which can explain the occurrence of many large submarine landslides worldwide.

METHODS

Seismic data was acquired using a GI Gun with 2x1.7 l chamber volume and a 500 m long analogue streamer hosting 80 channels (see the GSA Data Repository[1] for processing details). To correlate core lithology and seismic data we visually match the phases of a synthetic seismic trace calculated from core data (GRA density and initial constant p-wave velocity) with recorded seismic traces (see the Data Repository). The process of phase matching is iterative and includes vertical adjustment of the synthetic trace (‘stretching’ or ‘squeezing’), corresponding adaptation of the velocity profile, and recalculation of the synthetic trace using the updated velocity profile, all of which is integrated in the SynPAK module of The IHS Kingdom® software. Updated p-wave velocities are in the range of 1.3–1.8 m/s and thus reasonable for shallow marine sediments (Press, 1966).

RESULTS AND INTERPRETATION

Morphology of the Cap Blanc Slide Area

The Cap Blanc Slide is located at the continental slope off northern Mauritania. Swath bathymetric data covering parts of the slide show two main scarps with slope angles between 10-20° that delineate two failure surfaces (Fig. 1), which we refer to as ‘major’ slide for the larger slide and ‘minor’ slide to describe a smaller slide inside the bigger failed area. The scarp of the major slide can be traced from the southern boundary of the map toward a water depth of 1950 m. From here it kinks to the northwest and is visible for another 35 km. Inside the area delineated by the major scarp a smaller scarp

Publisher: GSA
Journal: GEOL: Geology
DOI:10.1130/G39892.1

extends to the northwest and southwest with heights of 25–50 m. The major and minor landslides intersect in the headwall area. The headwall of the major slide is 100 m high and increases to a height of almost 200 m where the two slides merge. The maximum seabed gradient in the area is 2.8°. The very smooth seafloor inside both slide areas indicates translational sliding along bedding parallel glide planes. The two glide planes locate at different stratigraphic depths. ODP Site 658 was drilled just south of the major sidewall inside the area evacuated by the major slide (Fig. 1).

Seismic Data and Stratigraphic Correlation

The slope parallel seismic line GeoB09–040 (Fig. 2) crosses the sidewalls of both the major (km 16) and the minor (km 5) slide as well as ODP Site 658 (km 11). In addition, another buried slide scar is imaged 1 km south of Site 658, at 10 km inline distance and 3.24 s TWT. None of the glide planes cut across stratigraphy, hence all slides failed parallel to the bedding. We identify glide planes as the top of the uppermost reflectors that are continuous across slide scars. Additional indication for glide planes are local disturbances in reflector continuity (e.g., at 13.8 km and 3.1 s TWT, 3.5 km and 3.28 s TWT) that represent slide debris on top of glide planes. Note that the respective reflectors traced into the unfailed sections are also termed glide planes. The glide plane of the major slide, GP_{MAJ}, does not appear as a particular strong reflection in the seismic data. A low amplitude reflector just below a high-amplitude reflector (H05) represents the horizon along which the minor slide moved, GP_{MIN}. The reflector associated with the glide plane of the buried scar, GP_{BUR}, is marked by a reflector that is of normal polarity in the failed section (south of the scarp) and of reversed polarity in the unfailed section. The thickness of the failed packages are 100 m for the major slide, 56 m for the minor slide

(Fig. 2, both calculated with sound velocity of 1500 m/s), and 31 m for the buried slide (estimated from the core). The horizontally layered shallow strata host nine prominent high-amplitude seismic reflectors that can be traced to ODP Site 658 (H01-H09, see Table DR1 in the Data Repository).

The core-seismic integration shows that the uppermost six seismic reflectors are evenly spaced in depth and time, with ~15 m of sediment, or ~100 ka, in between individual reflectors (Table DR1 in the Data Repository). The glide plane of the major slide correlates with a hiatus in the drill core and is likely responsible for removing the sediment deposited in the time interval between 731 and 1573 ka (Tiedemann, 1991). Ages of continuous reflectors across the scarp (i.e., the reflector directly on top of the glide planes, Fig. 2) represent sediment deposited after failure and thus give a minimum age of the respective slide.

Sedimentology of Glide Planes and Weak Layers

Figure 3 shows selected physical and sedimentological properties from ODP core 658 in relation to seismic horizons along line GeoB09–040. The nine prominent seismic reflections (H01-H09) correlate with 2–10 m thick sedimentary beds of low density, high porosity, high biogenic opal content, and high element log-ratios of silica to aluminum (ln(Si/Al), Fig. 3). These beds host high abundances of marine diatoms (siliceous microfossils), which were deposited during the terminations of glacial periods (Meckler et al., 2013; Tiedemann, 1991).

The weak layer of the major slide (formerly covering GP_{MAJ}) has most likely vanished with the slide material. In contrast, the weak layers for the minor and buried slides are present in the ODP core because the site is located outside of their scar areas

(Figs. 1, 3). The glide plane of the minor slide, GP_{MIN}, in ~69 m depth lies just below seismic reflector H05. H05 coincides with a ~2.5 m thick diatom ooze layer (Tiedemann, 1991) characterized by a density decrease to 1.28 g/cm^3 and high porosity of 72%. The log-ratio of Si and Al shows a prominent peak of 3.5 between 65 and 67 m, in line with an opal content maximum of 40%. The sediment covering GP_{MIN} yields a large clay fraction of 77% extending from 60 to 66 m, below which the clay content drastically decreases to 20% at 68 m.

The glide plane of the buried slide, GP_{BUR}, is located at ~183 m in the ODP core. Between 177 m and 181 m core depth a density minimum of 1.25 g/cm^3 and peaks in porosity of 66% as well as opal content of 54% reveal another diatom-rich layer. Clay content is almost 80% (Fig. 3). The occurrence of a 10 m thick package of low density diatom ooze also explains the reversed polarity reflector overlying the inferred glide plane in the unfailed part of the slope (Fig. 2).

In summary, both glide planes appear very close to the interface of layers of diatom oozes with increased biogenic opal content and clay-rich sediment on top. Other diatom-rich layers away from glide planes (H01-H04, H06, H07, H09) are covered by coarser sediment (Fig. 3). However, owing to the limited vertical seismic resolution of 7.5 m and uncertainties in the core-seismic correlation we cannot exactly determine whether the sediment failed below, inside or above the thin opal rich layers. The weak layer could therefore be the diatom ooze, the overlying clay-rich sediment, or the interface between both layers.

DISCUSSION

Core-seismic integration shows that the glide planes for the Cap Blanc Slide coincide with diatom oozes topped by clay. Diatoms are siliceous microfossils and their presence is known to significantly influence the geotechnical properties of sediments, even in minor amounts. Water content, permeability, compressibility, and angle of friction all increase with the amount of diatoms (Bryant et al. 1981, Tanaka and Locat, 1999; Wiemer et al., 2017). High friction angles suggest that diatom ooze would rather act as a barrier to failure rather than a weak layer. However, the diatoms' high compressibility may lead to compaction disequilibrium during burial. Urlaub et al. (2015) numerically modeled the burial of a layer with compressibility similar to that measured for diatom oozes (i.e., C_c>1.04) and showed that deposition of sedimentation with rates similar to those encountered off Cap Blanc (>0.15 m/ky) could cause sufficient excess pore pressure to destabilize a 2° slope. In addition to the accumulation of excess pore pressure due to rapid decrease in pore space during compaction, diatoms contain large amounts of intraparticle water stored in their hollow shells and skeletal pores, which is released once the confining stress exceeds a critical threshold and particles crush. Given that intraparticle water in diatom oozes may be as high as 15% of its dry weight this process could release significant amounts of excess fluid (Tanaka and Locat, 1999). Kokusho and Kojima (2012) showed that the presence of a liquefiable silty layer, such as diatom ooze, at a lower permeability boundary can generate accumulation of water, which could generate a failure surface. Based on these considerations and our results from core-seismic integration we suggest that for the Cap Blanc Slide a bedding sequence of diatom oozes capped by clay may form an induced weak layer (Locat, 2014). We propose the following conceptual model to explain landslides in diatom-rich sediment:

1. Widespread deposition of large amounts of diatoms in hemipelagic sediment is followed by deposition of clay. As a consequence of continuously increasing overburden, the diatom ooze consolidates by vertical drainage of excess pore fluid and subsequent volume loss. Hydrostatic conditions are maintained until the drainage path becomes too long or the permeability of the overlying sediment becomes too low for the excess pore fluid to drain.
2. Excess pore fluid is trapped at the interface between the ooze and the overlying clay. As burial and the release of intraparticle water continue, excess pore pressure constantly increases causing the shearing resistance and the shear stress to increase at different rates with increasing depth.
3. When the shear stress exceeds the shear strength of the ooze or the clay slope failure occurs. Recalling the high frictional resistance of diatom ooze, failure is more likely to take place in the clay than in the ooze. However, the presence of diatom ooze is crucial as it provides an effective source of pore fluid.

The proposed failure mechanism differs to what has been suggested in previous studies that reported on a link between opal and submarine landslide occurrence. Volpi et al. (2003) and Davies and Clark (2006) suggested that water released by the transition of opal-A to opal-CT caused submarine landslides. However, this diagenetic alteration acts at 300–800 m below seafloor, which is much deeper than the glide planes of mega-slides off NW Africa (50–150 m, Krastel et al. 2012) and most submarine landslides on continental slopes in general (10–100 m, Masson et al., 2010).

Potential of Diatom Ooze as a Global and Widespread Weak Layer

Diatom oozes typically occur in the southern and tropical oceans, as the burial of biogenic opal relies on sufficient supply of silicate and thus high diatom productivity in surface waters. Diatom blooms are also common in upwelling areas along continental margins, where deep, nutrient-rich cold water rises toward the surface. In particular, during glacial times, strong winds and intensified upwelling favors productivity. In the subtropical North Atlantic, a reduction in the formation of silicate poor glacial North Atlantic Intermediate Waters during deglaciations allowed underlying silicate rich deeper water to increase the silicate supply to the surface ocean, which led to the formation of diatom oozes at ODP Site 658 and other places along the entire Western African continental margin (Meckler et al., 2013). It therefore seems plausible that shallow (<100 m) high amplitude seismic reflectors observed in high resolution seismic data along this margin represent diatom ooze layers in contact with hemipelagic sediment. The potential critical role of diatom oozes not only for the Cap Blanc but also for the generation of the Sahara, Mauritania, and Dakar slides is evident as the glide planes coincide with such reflectors (Antobreh and Krastel, 2007, and the Data Repository).

In the Arctic Ocean, Kristoffersen et al. (2007) combine seismic data with IODP Site M0004 to identify the interface between diatom ooze and overlying silty clay as the glide planes for seven landslides on the Lomonosov Ridge. Pittenger et al. (1989) and Busch and Keller (1982) have considered diatom oozes as potentially unstable at the Vøring Plateau, Norway, and in one of the largest upwelling areas worldwide, the Peruvian continental margin. The lowermost headwall in the Storegga Slide complex formed in siliceous biogenic oozes, potentially leading to the initiation of the entire Storegga Slide (Riis et al. 2005). Our study provides direct evidence for diatom ooze as weak layer for the Cap Blanc Slide. Combined with the above considerations from other continental slopes, this suggests that burial and loading of diatom oozes covered by clay could be an important preconditioning factor for many submarine landslides globally. To improve understanding of this process and due to the large variety of diatom species, which may have fundamentally different mechanical behaviors, future work should focus on analyzing the nature and evolution of the microfossil skeletons in the oozes that are suspected to act as weak layers.

ACKNOWLEDGMENTS

We thank the captain and crew of RV Maria S. Merian cruise 11/2, as well as the watchkeepers for seismic and hydroacoustic systems. Sascha Fricke is acknowledged for seismic data processing. We thank A. Georgiopoulou, Tanaka, J. Locat, A. Camerlenghi, and three anonymous reviewers for their detailed comments, which substantially improved the paper.

REFERENCES CITED

Antobreh, A.A., and Krastel, S., 2007, Mauritania Slide Complex: morphology, seismic characterisation and processes of formation: International Journal of Earth Sciences, v. 96, p. 451–472, https://doi.org/10.1007/s00531-006-0112-8.

Bondevik, S., Lovholt, F., Harbitz, C., Mangerud, J., Dawson, A., and Svendsen, J.I., 2005, The Storegga Slide tsunami-comparing field observations with numerical simulations: Marine and Petroleum Geology, v. 22, p. 195–208, https://doi.org/10.1016/j.marpetgeo.2004.10.003.

Bryant,W.R., Bennett, R.H., and Katerman, C.E., 1981, Shear strength, consolidation, porosity, and permeability of oceanic sediments, *in*: Emiliani, C., ed., The Sea, J.Wiley & Sons, NewYork, , v. 7, p. 1555-1616.

Busch, W.H., and Keller, G.H., 1982, Consolidation characteristics of sediments from the Peru-Chile continental margin and implications for past sediment instability: Marine Geology, v. 45, p. 17–39, https://doi.org/10.1016/0025-3227(82)90178-5.

Dan, G., Sultan, N., and Savoye, B., 2007, The 1979 Nice harbour catastrophe revisited: Trigger mechanism inferred from geotechnical measurements and numerical modelling: Marine Geology, v. 245, p. 40–64, https://doi.org/10.1016/j.margeo.2007.06.011.

Davies, R.J., and Clark, I.R., 2006, Submarine slope failure primed and triggered by silica and its diagenesis: Basin Research, v. 18, p. 339–350, https://doi.org/10.1111/j.1365-2117.2006.00297.x.

Kokusho, T., and Kojima, T., 2002, Mechanism for postliquefaction water film generation in layered sand. J Geotech Geoenviron Eng, v. 128, p.129–137..

Krastel, S., Wynn, R.B., Georgiopoulou, A., Geersen, J., Henrich, R., Meyer, M., and Schwenk, T., 2012, Large-scale mass wasting on the Northwest African Continental Margin: Some general Implications for mass wasting on passive continental margins, *in* Yamada, Y., et al., eds., Submarine Mass Movements and Their Consequences: Dordrecht, Netherlands, Springer, Advances in Natural and Technological Hazards Research, v. 31, p. 189–199, doi:10.1007/978-94-007-2162-3_17.

Kristoffersen, Y., Coakley, B.J., Hall, J.K., and Edwards, M., 2007, Mass wasting on the submarine Lomonosov Ridge, central Arctic Ocean: Marine Geology, v. 243, p. 132–142, https://doi.org/10.1016/j.margeo.2007.04.012.

Kvalstad, T.J., Andresen, L., Forsberg, C.F., Berg, K., Bryn, P., and Wangen, M., 2005, The Storegga Slide: Evaluation of triggering sources and slide mechanics: Marine and Petroleum Geology, v. 22, p. 245–256, https://doi.org/10.1016/j.marpetgeo.2004.10.019.

L’Heureux, J.-S., et al., 2012, Identification of Weak Layers and Their Role for the Stability of Slopes at Finneidfjord, Northern Norway, *in* Yamada, Y., et al., eds., Submarine Mass Movements and Their Consequences: Dordrecht, Netherlands, Springer, Advances in Natural and Technological Hazards Research, v. 31, p. 321–330, doi:10.1007/978-94-007-2162-3_29.

Locat, J., 2014, Weak Layers: Their Definition and Classification from a Geotechnical Perspective, *in* Krastel, S., et al., eds., Submarine Mass Movements and Their Consequences: Dordrecht, Netherlands, Springer, Advances in Natural and Technological Hazards Research, v. 37, p. 3-12, https://doi.org/10.1007/978-3-319-00972-8.

Masson, D.G., Harbitz, C.B., Wynn, R.B., Pedersen, G., and Løvholt, F., 2006, Submarine landslides: Processes, triggers and hazard prediction: Philosophical Transactions of the Royal Society A, v. 364, p. 2009–2039, https://doi.org/10.1098/rsta.2006.1810.

Masson, D.G., Wynn, R.B., and Talling, P.J., 2010, Large Landslides on Passive Continental Margins: Processes, Hypotheses and Outstanding Questions, *in* Mosher, D.C., et al., eds., Submarine Mass Movements and Their Consequences: Dordrecht, Netherlands, Springer, Advances in Natural and Technological Hazards Research, v. 28, p. 153–165, doi:10.1007/978-90-481-3071-9_13.

Meckler, A., Sigman, D., Gibson, K., François, R., Martinez-Garcia, A., Jaccard, S., Röhl, U., Peterson, L.C., Tiedemann, R., and Haug, G., 2013, Deglacial pulses of deep-ocean silicate into the subtropical North Atlantic Ocean: Nature, v. 495, p. 495–498, https://doi.org/10.1038/nature12006.

Milliman, J.D., and Syvitski, J.P.M., 1992, Geomorphic/tectonic control of sediment discharge to the ocean: The importance of small mountaineous rivers: The Journal of Geology, v. 100, p. 525–544, https://doi.org/10.1086/629606.

Pittenger, A., Taylor, E., and Bryant, W.R., 1989, The influence of biogenic silica on the geotechnical stratigraphy of the Voring Plateau, Norwegian Sea, *in* Eldholm, O., et al., eds., Proceedings of the Ocean Drilling Program, Scientific Results: College Station, Texas, Ocean Drilling Program, v. 104, p. 923–940, doi:10.2973/odp.proc.sr.104.145.1989.

Press, F., 1966, Section 9: Seismic velocities: Geological Society of America Memoir 97, p. 195–218.

Riis, F., Berg, K., Cartwright, J.A., Eidvin, T., and Hansch, K., 2005, Formation of huge crater structures in ooze sediments in the Norwegian Sea. Possible implications for the triggering of the Storegga Slide: Marine and Petroleum Geology, v. 22, p. 257-273, httpsdoi:10.1016/j.marpetgeo.2004.10.023.

Tanaka, H., and Locat, J., 1999, A microstructural investigation of Osaka Bay clay: The impact of microfossils on its mechanical behaviour: Canadian Geotechnical Journal, v. 36, p. 493–508, https://doi.org/10.1139/t99-009.

Tiedemann, R., 1991, Acht Millionen Jahre Klimageschichte von Nordwest Afrika und Paläo-Ozeanographie des angrenzenden Atlantik: Hochauflösende Zeitreihen von ODP-Sites 658–661 [Ph.D. Thesis]: Kiel, Germany, University of Kiel, 127 p.

Urlaub, M., Talling, P.J., Zervos, A., and Masson, D., 2015, What causes large submarine landslides on low gradient (<2°) continental slopes with slow (~0.15 m/kyr) sediment accumulation?: Journal of Geophysical Research. Solid Earth, v. 120, p. 6722–6739, https://doi.org/10.1002/2015JB012347.

Voight, B., Janda, R.J., and Glicken, H., 1983, Nature and mechanics of the Mount St. Helens rockslide-avalanche of 18 May 1980: Geotechnique, v. 33, p. 243–273, https://doi.org/10.1680/geot.1983.33.3.243.

Volpi, V., Camerlenghi, A., Hillenbrand, C.-D., Rebesco, M., and Ivaldi, R., 2003, Effects of biogenic silica on sediment compaction and slope stability on the Pacific margin of the Antarctic Peninsula: Basin Research, v. 15, p. 339–363, https://doi.org/10.1046/j.1365-2117.2003.00210.x.

Wiemer, G., Dziadek, R., and Kopf, A., 2017, The enigmatic consolidation of diatomaceous sediment: Marine Geology, v. 385, p. 173–184, https://doi.org/10.1016/j.margeo.2017.01.006.

FIGURE CAPTIONS

Figure 1. Bathymetric map of the Cap Blanc Slide showing the scarps of a larger ('major') and a smaller ('minor') landslide. ODP Site 658 marked by the red dot was drilled inside the failed area of the major slide. The black solid line shows the location of seismic profile GeoB09–040. The inset shows GEBCO bathymetry of the Northwest African continental slope (WS = Western Sahara, MAU = Mauritania, SN = Senegal) including the location of the main figure (red rectangle).

Figure 2. Seismic reflection line GeoB09–040 across the Cap Blanc Slide area and ODP Site 658 (green vertical line). Colored arrows indicate the glide planes corresponding to the minor slide (purple), the major slide (red) and the buried slide (blue). Nine prominent high-amplitude reflectors are termed H01-H09. See Figure 1 for location of the profile and the GSA Data Repository (see footnote 1) for an enlarged and uninterpreted version of the profile.

Figure 3. Core data from ODP Site 658 from left to right: bulk density, ρ_{GRA} (from Gamma Ray Attenuation measurements, filtered for realistic values); porosity (black) and water content (gray) from Moisture And Density measurements; biogenic silica equivalent to opal content of the sediment fraction >2 μm determined by density separation, $bSiO_2$ (black), and element log-ratio of silica to aluminum, ln(Si/Al) (gray); clay content (i.e. sediment fraction <2 μm). X-ray fluorescence scanning-derived element log-ratio of silica to aluminum counts (ln(Si/Al), Meckler et al. 2013) is a proxy for sediment opal content. Average sample distances are 1.5 m (0–100 m) and 2.5 m (100–200 m). Seismic reflectors H01-H09 are shaded in gray with an uncertainty of ± 2 m

Publisher: GSA
Journal: GEOL: Geology
DOI:10.1130/G39892.1

owing to the vertical resolution of the seismic data, i.e., ¼ of the wavelength. Dashed lines indicate the inferred glide planes for the minor (purple), the major (red) and the buried (blue) slides.

[1]GSA Data Repository item 2018xxx, description of methodology and high-resolution image of the seismic transects without interpretation, is available online at http://www.geosociety.org/datarepository/2018/ or on request from editing@geosociety.org.

Figure 1

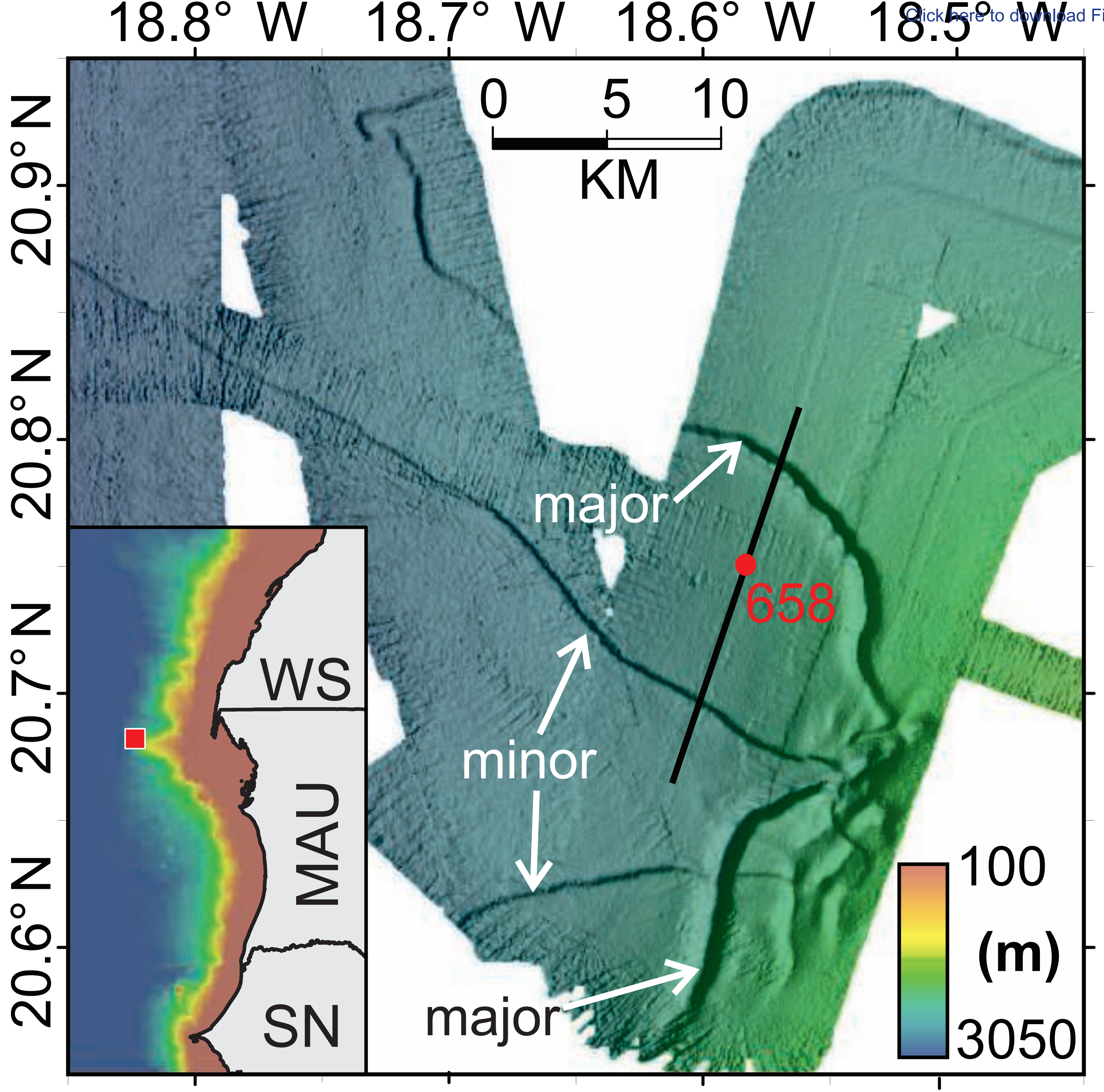
18.8° W
18.7° W
18.6° W
18.5° W
20.9° N
20.8° N
20.7° N
20.6° N
0
5
10
KM
major
658
minor
major
100
(m)
3050
WS
MAU
SN

Figure 2

Click here to download Figure FIG2.eps

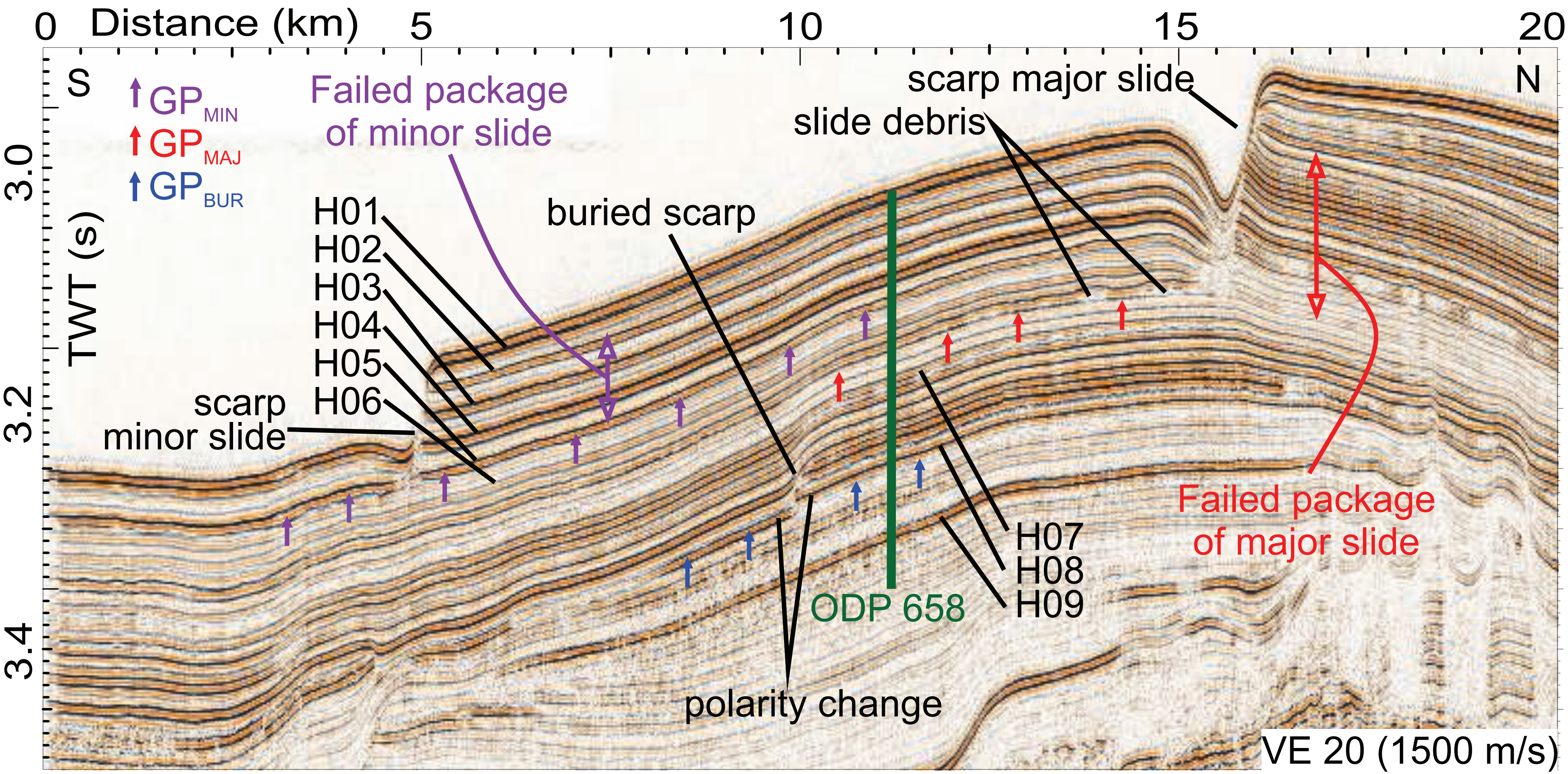

Figure 3

Click here to download Figure FIG3.eps

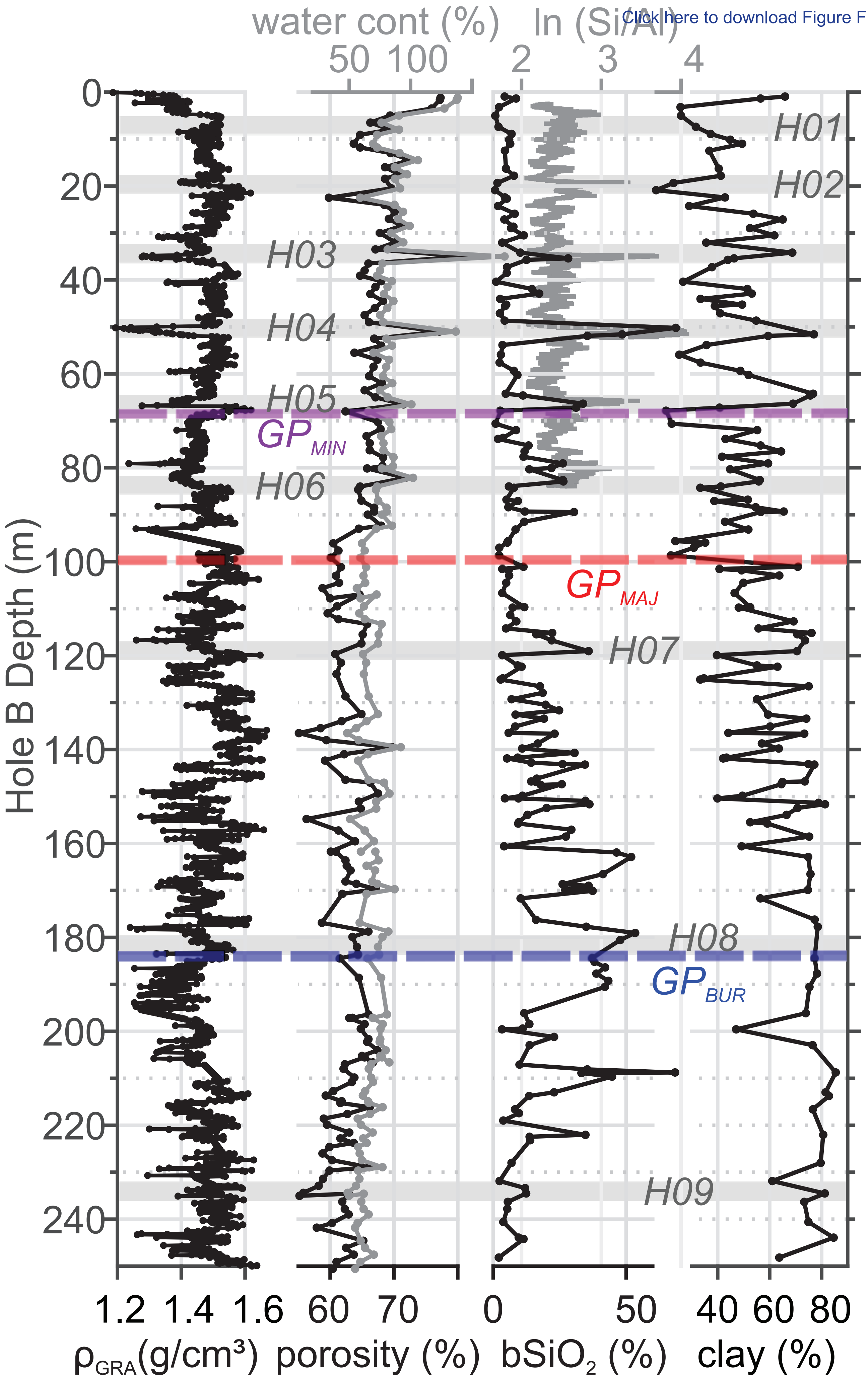

Text and figures for GSA Data Repository to accompany

"Diatom ooze: Crucial for the generation of submarine mega-slides"

by Urlaub, M., Geersen, J., Krastel, S., and Schwenk, T.

Methodology

Acoustic data

Multibeam bathymetric data was collected during cruise MSM11/2 in 2009 with the hull-mounted Kongsberg Simrad symstem EM120. Processing was carried out with open source software MB-System and Fledermaus Pro (QPS) to create a grid with 50 m resolution. During the same leg 2D high-resolution multichannel seismic data were acquired using a GI Gun with 2x 1.7 l chamber volume (main frequencies between 100 and 200 Hz) and a 500 m long analogue streamer hosting 80 channels. Seismic data processing was carried out with VISTA (Schlumberger) and included binning with 5 m size, trace editing, NMO correction and stacking as well as migration. The data is capable of resolving layers with thickness as low as 7m.

Core-seismic integration

We calculate the synthetic seismogram for ODP site 658 based on densities determined from Gamma-Ray-Attenuation (GRA) and a constant p-wave velocity of 1500 m/s. Due to expansion of free gas in the sediment during core recovery reliable measurements of p-wave velocity are only available for the upper 10 m of the core (Ruddiman et al., 1988). However, velocity values normally scatter around a mean trend and variations in marine surface sediments do not exceed 5%, whereas density variations are much higher (>20%) within these sediments (e.g. Breitzke, 2000). Velocity data are thus less important for the calculation of reflection coefficients in this specific environment. Therefore, an initial constant p-wave velocity of 1500 m/s was used for the whole length of the core.

GRA density values are available for ODP cores 658A, B and C at an interval of about 0.6 cm including several gaps of up to a few meters. Although core A represents the longest record, values for the upper 165 m were taken from core B as it contains less and smaller gaps. Problems with GRA -density measurements occur where the core liner is not entirely filled with sediment or where there is gas expanding in the sediment. In situ this gas was most likely dissolved in the pore water as the high resolution seismic data does not show any evidence for free gas. Already 1-3% of free gas would reduce the P-wave velocity significantly enough to create a bright spot or blanking in the seismic data (considering the high frequencies of our data around 100 Hz) (e.g. Singh et al., 19930 or Minshull et al., 1994). Hence to avoid density values affected by free gas (and thus conditions that are not representative to those in the seafloor) the density data is filtered to eliminate values lower than 1.025 g/cm³, equal to the density of seawater (a lower value may only occur if gas is present in the pore space). We also apply a high-cut filter for values larger than 2.7 g/cm³ (representing the density of clay or silt particles). Furthermore, the central value of a running average of 300 data points is compared to the mean of the data window. For differences greater than 0.25 g/cm³ the value is deleted. We then calculate standard deviations for a moving 50 points window. Each value is compared to the mean of the 50 neighboring points and if the difference is larger than twice the standard deviation for the window it is eliminated. The filtering of GRA - density lead to a reduction of data points from 38516 to 33165 values. Filtering also caused gaps in the density data in some locations (e.g. between 97 and 100 mbsf and 209 and 212 mbsf). In order to avoid artificial reflectors produced by these data gaps we linearly interpolated to the next density value. The filtered and interpolated data was finally used for the calculation of a synthetic seismogram. As the part below 275 m is mainly represented by two large gaps, density data was only used above this depth. Finally, a smoothing of the density record was achieved by the use of a 10 cm running average. To avoid unrealistic reflection coefficients the data was linearly interpolated at places where gaps in the final density record occurred.

Reflection coefficients are calculated from the density values and constant velocity and convolved with a wavelet, which approximates the seismic signal observed in the field. As a source wavelet a standard Ricker wavelet (Ricker, 1953) was preferred over a wavelet extracted from seismic traces near the borehole. The synthetic wavelet appears smoother than the recorded one and has proven to be more useful for a visual correlation of measured and synthetic data. The wavelet contains a frequency of 100 Hz corresponding to the dominant frequency of the GI-gun. The sampling rate is 250 µs which is equivalent to the seismic profile. For the core-seismic integration we use the SynPAK module in the IHS Kingdom® software. The synthetic seismogram is shifted, stretched or squeezed to match the nearby seismic survey traces and the interval velocities are adapted correspondingly. The software recalculates the synthetic using the updated velocity profile. During stretching and squeezing great care was taken that the updated velocities are in a reasonable range for marine sediments (1.2 - 4 m/s, Press 1966).

TABLE S1 High amplitude reflectors, glide planes, and post-failure reflectors providing minimum slide ages identified in the seismic line and tied in to ODP core 658 as a result of core-seismic integration. TWT is two-way-traveltime of individual reflectors at the borehole. We use the age model by Tiedemann (1991).

Seismic horizon	TWT (s)	Core depth (m)	Age (ka)
H01	3.029	7	50
H02	3.046	20	149
H03	3.065	35	247
H04	3.088	51	342
H05	3.107	66	434
H06	3.128	83	563
H07	3.174	119	1800
H08	3.244	182	2500
H09	3.308	234	2960

GP_{MIN}	3.112	69	434
GP_{MAJ}	3.151	100	1573
GP_{BUR}	3.248	183	2500
$Post_{MIN}$	3.046	20	149
$Post_{MAJ}$	3.151	100	731
$Post_{BUR}$	3.215	154	2300

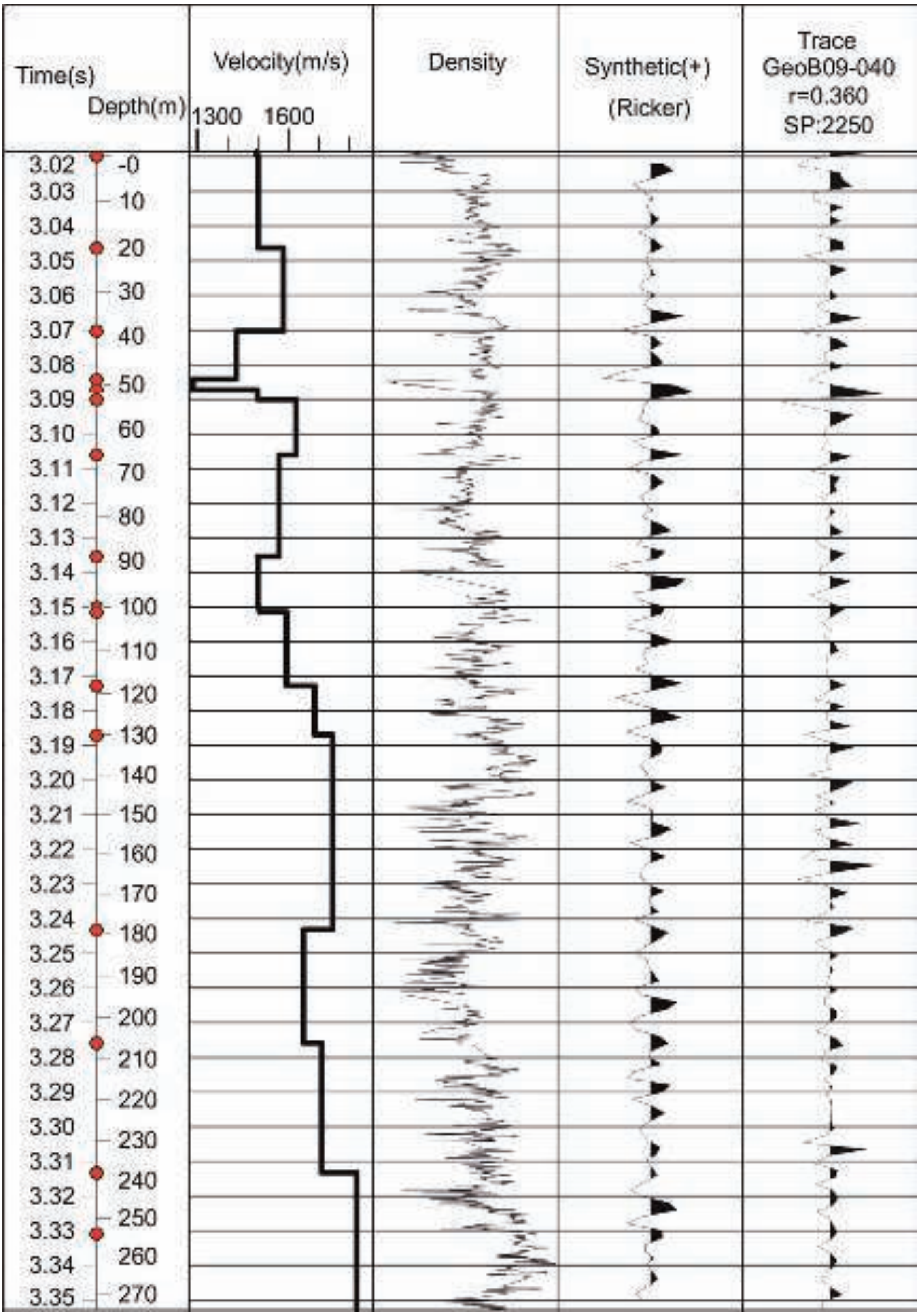

Figure S1: *Core seismic integration correlation panel. The synthetic seismogram was shifted, stretched or squeezed to match the nearby seismic survey traces and the interval velocities are adapted correspondingly.The synthetic seismogram is recalculated using the new velocity profile after each adjustment.*

References

Breitzke, M. (2000). Acoustic and elastic characterization of marine sediments by analysis, modeling, and inversion of ultrasonic P wave transmission seismograms. Journal of Geophysical Research: Solid Earth, 105(B9), 21411-21430.

Minshull, T.A., Singh, S., Westbrook, G.K. (1994). Seismic velocity structure at a gas hydrate reflector, offshore western Colombia, from full waveform inversion. Journal of Geophysical Research: Solide Earth, 99(B3), 4715-4743.

Press, F. (1966). Section 9: Seismic velocities. Geological Society of America Memoirs, 97, 195-218.

Ricker, N. (1953). Wavelet contraction, wavelet expansion, and the control of seismic resolution. Geophysics, 18(4), 769-792.

Ruddiman, W., Sarnthein, M., Baldauf, J., et al., 1988. Proc. ODP, Init. Repts., 108: College Station, TX (Ocean Drilling Program).

Singh, S., Minshull, T.A., Spence, G.D. (1993). Velocity Structure of a Gas Hydrate Reflector. Science, 260, 5105, 204-207.

Tiedemann, R., 1991. Acht Millionene Jahre Klimageschichte von Nordwest Afrika und Paläo-Ozeanographie des angrenzenden Atlantik: Hochauflösende Zeitreihen von ODP-Sites 658–661. [Ph.D. thesis]: University of Kiel, Germany, 127 p.

Additional figures

Figure S2: Seismic line GeoB09-040 uninterpreted and at high resolution.

Figure S3: Seismic line GeoB03-017 downslope that crosses line GeoB09-040 at a right angle at ODP Site 658.

Figure S4: High resolution seismic lines showing high amplitude reflectors that are typical for the shallow sediments on the continental slope of Northwest Africa and that coincide with landslide scars for A) Sahara Slide, B) Mauritania Slide, and C) Dakar Slide.

Supplemental figure 2

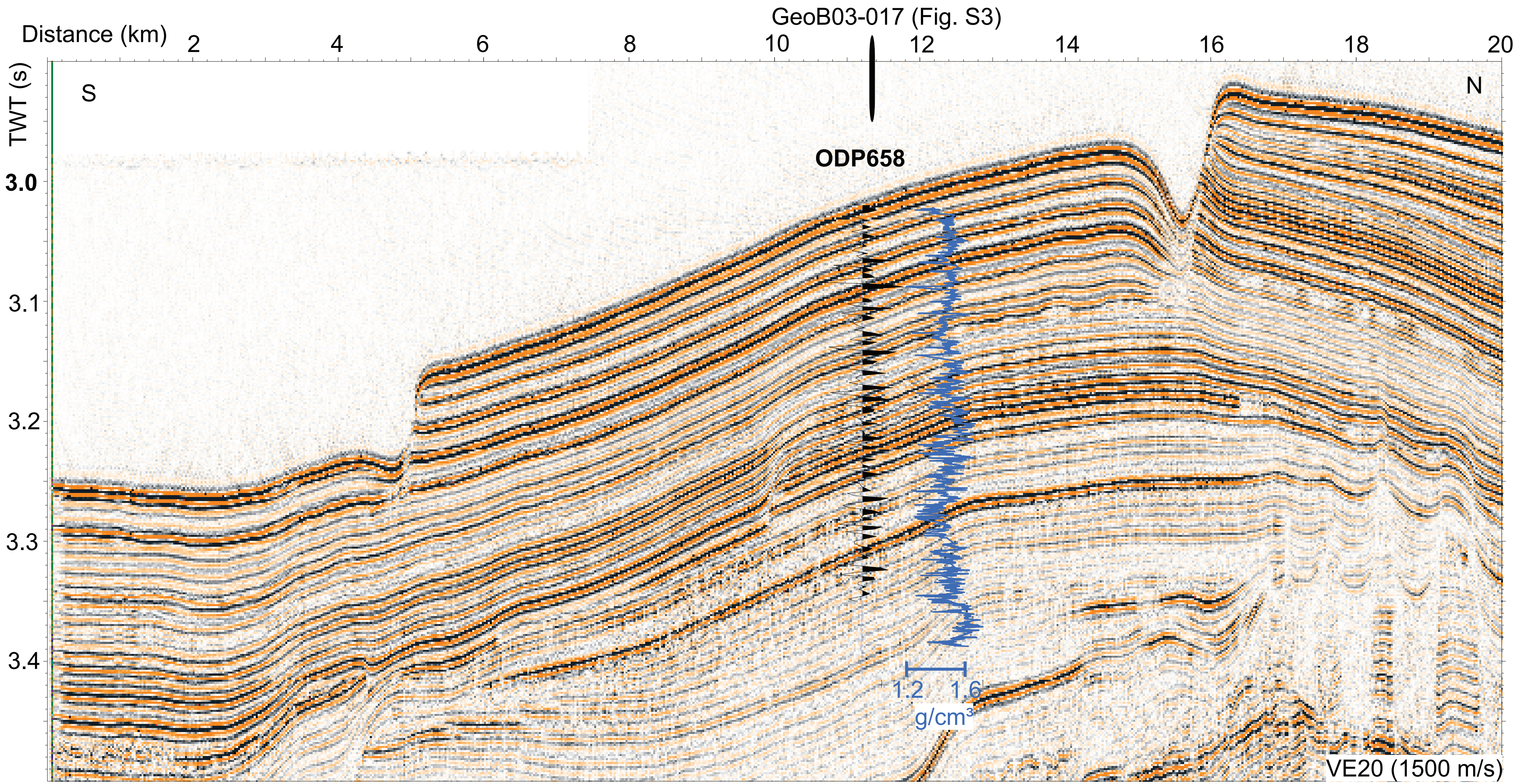

Supplemental figure 3

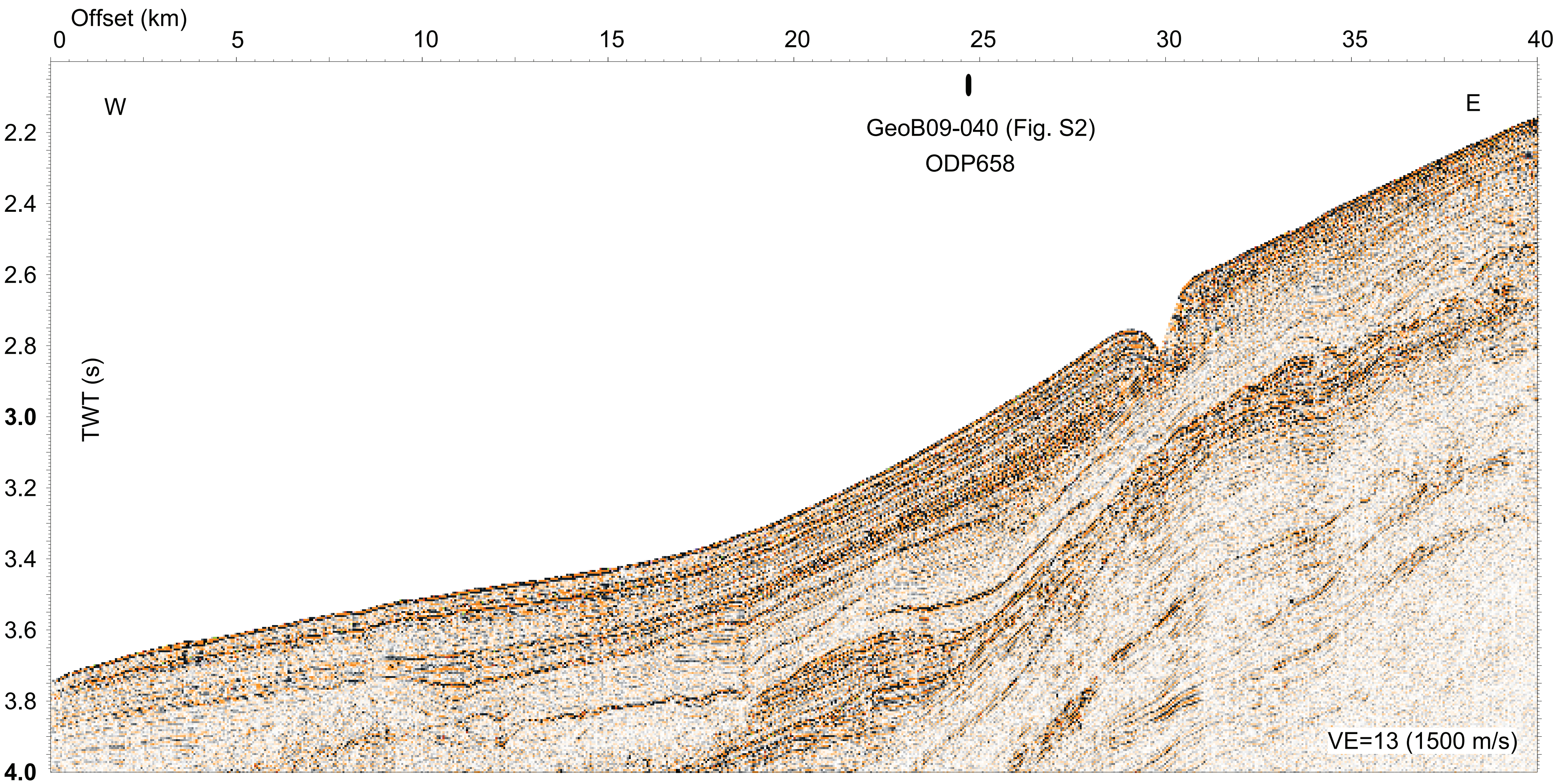

Supplemental figure 4 Click here to download Supplemental file FigS4.pdf